Macro- and microphysical characteristics of rain cells observed during SOS-CHUVA

M. A. Cecchini[1], M. A. F. Silva Dias[1], L. A. T. Machado[2], C. A. Morales[1], and T. Biscaro[2]

[1]Instituto de Astronomia, Geofísica e Ciências Atmosféricas (IAG), Universidade de São Paulo (USP), São Paulo, Brazil.

[2]Centro de Previsão de Tempo e Estudos Climáticos (CPTEC), Instituto Nacional de Pesquisas Espaciais (INPE), Cachoeira Paulista, Brazil.

Corresponding author: Micael Cecchini (micael.cecchini@usp.br)

Key Points:

- Holistic view of convective rain cells in Campinas, Brazil using X-band radar.
- The importance of the macroscale context for microphysical analyzes is explored.
- Polarimetric and gamma DSD variables are studied in a Lagrangean way for rain cells.

Abstract

In this study we present a methodology to study the properties of convective precipitation in a holistic way. We apply a tracking algorithm to X-band radar retrievals to store rain cells properties in a Lagrangean framework. The Center of Activity (COA), the altitude with the highest contribution to the cell's Vertically Integrated Liquid (VIL), is presented as a new perspective to study convective clouds. It is shown that the combination of COA and VIL provides a useful phase space to compare the properties of different rain cells. In our methodology, rain cells present high COA (around 4.0 km to 4.5 km) and high VIL (~3.0 kg m^{-2}) upon detection and evolve towards lower COA and VIL values throughout the lifecycle. The COA-VIL space is also used to constrain the microphysical study of the cells. Averaged polarimetric variables and gamma Droplet Size Distribution (DSD) parameters indicate that collection, melting and evaporation processes are almost in balance at COA independently of the rain cells lifecycle stage. High COA and negative DSD shape parameters (μ) at COA were found 10 minutes before peak accumulated rainfall in low levels and are also likely associated to lightning activity and differential reflectivity (Z_{dr}) columns. Overall, the results presented here can help nowcasting applications by providing expected microphysical characteristics from COA-VIL calculations. Contrary to microphysical retrievals, computations of COA and VIL do not depend on dual polarization.

Plain Language Summary

In this study we looked for rain properties that are shared among different rain occasions during the summer of 2016/7 around Campinas city in Southeast Brazil. By following each case with a weather radar, we were able to store rain properties throughout their life cycle as well as in different altitudes. It was found that the altitude with the highest rain mass, together with the overall water mass amount, are two key properties that can help categorize rain occasions. When most of the water is relatively high in the clouds, e.g. 4 km high, the clouds were found to be in their most developed stage, where lightning activity is expected to start. About 10 minutes after this point, the bulk of the rain reaches lower levels (2 km in our methodology). This process is modulated by the overall rain water mass generated by the clouds, meaning that both properties should be used together for a more complete view. Additionally, this approach provides a context for more detailed studies of precipitation, where the processes responsible for rain formation are the main focus. We propose that the results presented here can help both operational forecasters and weather researchers to better anticipate intense rain occasions and the associated potential damages for society such as strong winds and lightning activity.

1 Introduction

Convective clouds are one of the primary focus of meteorological studies given their importance to the overall climate and their effects on human society functioning. When severe convective clouds, either individually or in groups, act over populated areas, both human and patrimonial damage may follow. Perhaps the primary example are flood occasions, which have both direct and indirect effects – the first related to the elevation of rivers water levels and the latter to the dissemination of diseases by polluted rivers (Beyer, 1974). The progressive urbanization process, especially unorganized urbanization, intensifies the problem by limiting the surface infiltration capacity (Stevaux et al., 2009). Additionally, convective systems may also produce lightning activity, hail and windstorms and can disrupt cities electricity distribution. Hailfall, in particular, have a lot of damage reports in Brazil (Martins et al., 2017). Therefore, understanding the nature of convective systems is crucial in order to minimize their effects and improve the response time by providing early warnings.

Recent efforts to further the knowledge of convective clouds in Brazil were made around the deployment of the CHUVA project (the word for "rain" in Portuguese, an acronym for Cloud Processes of the Main Precipitation Systems in Brazil: A Contribution to Cloud-Resolving Modeling and to the Global Precipitation Measurement (GPM), Machado et al., 2014). Calheiros and Machado (2014) reported on the early results of the campaign, where precipitation clouds in different regions in Brazil were compared. They found that clouds over Southeast Brazil present the most active mixed layer, which may be due to enhanced pollution of the highly urbanized region. The CHUVA project lead to the implementation of a new experimental campaign focused primarily on Southeast Brazil named SOS-CHUVA (Nowcasting of intense thunderstorms and understanding of the physical processes inside clouds: the SOS-CHUVA (Severe Weather Observation System)). The overall aim of SOS-CHUVA is to study deep convective clouds around the region of Campinas (São Paulo state) using ground-based instrumentation including a X-band radar used in the present study.

Here we will report on X-band radar measurements during the summer of 2016/7 with the focus to highlight holistic characteristics of the precipitating clouds around Campinas. The progressive improvement of model resolutions and experimental capabilities have elucidated the highly complex nature of the macro- and microphysical properties of convective clouds. These have prompted the development of new strategies that aim to find key properties that synthesize the systems characteristics in a holistic way. An example is introduced in Heiblum et al. (2016a), where the authors use large eddy simulations to analyze warm cumulus fields in a 2-dimensional phase space defined by each cloud's center of gravity (COG) altitude and their respective average liquid water path (LWP) or total amount of water mass. The authors highlight several cloud properties in the phase space, showing patterns typical of the growing or dissipating (both reversible and irreversible) stages, precipitating clouds, mergers and splits, for example. Therefore, it can be used as a tool to compare different clouds life cycles while interpreting the underlying physical and morphological aspects. One example of application of the COG-LWP phase space is provided in Heiblum et al. (2016b). The authors studied aerosol-cloud interactions in the phase space and showed that aerosols significantly alter the shapes and trajectories in it according to the underlying physical processes being affected. Overall, the COG tends to rise with aerosol loading in warm clouds because of both microscale processes such as decreased droplet terminal velocities and increased updraft speeds as well as macroscale effects in the increased environmental instability. The aerosol effect on the COG was further explored in Chen et al. (2017), where the effects in the up- and downdrafts were quantitatively compared (e.g. increased droplet mobility and decreased terminal speed, respectively). Dagan et al. (2018) studied how the aerosol effect on the warm phase affected the mass transport to deeper systems that grow above the freezing level. They found that increased pollution tends to increase mass transport both up- and downwards through the freezing level as a result of the higher COG and the more active mixed phase. Preliminary SOS-CHUVA results indicate that aerosol concentrations revolve around a few thousands per cm^{-3}, which is consistent with urban centers environments. Therefore, it is expected that clouds analyzed here resemble the most polluted cases of the literature discussed above.

In terms of cloud microphysics, Cecchini et al. (2017) introduced the so-called Gamma phase space to provide a holistic way to analyze processes inside individual clouds. The authors fitted Gamma curves to aircraft in-situ measurements of cloud droplet size distributions (DSD) and used the three parameters - intercept, shape and curvature - to construct the phase space. Therefore, every DSD was viewed as a point in a 3D subspace and their evolution as trajectories. They argue that processes such as condensation and collision-coalescence produce specific patterns in the phase space, which could be used to both validate model calculations and to develop new parameterizations that also rely on the Gamma DSD approximation. In the present study, we will apply both concepts of macro- and microscale phase spaces to generate a framework adequate to holistically study the convective systems measured during SOS-CHUVA. Because the experimental approach is significantly different than the studies mentioned here, several practical and theoretical adaptions were necessary as discussed in the next sections.

Here we introduce the Center of Activity (COA) that is a measure of the clouds altitude level with the highest amount of water mass as seen from radar reflectivity measurements. This property, together with the Vertically Integrated Liquid (VIL) will be used as a macroscale constraint similar to the phase space introduced in Heiblum et al. (2016a). This approach provides a new perspective on the study of clouds lifecycle from radar measurements while providing a framework to analyze individual or groups of cases. Within this context, microphysical properties will be analyzed from the polarimetric radar measurements and Gamma DSD parameters estimates.

Section 2 provides information on data handling and analysis methodology overview. The results are shown in Section 3, while the conclusions are provided in Section 4.

2 Methodology

2.1 Radar data

The X-band dualpol radar was operated at 9.345 GHz with a 1.3° beamwidth at -3 dB and in a simultaneous transmission and reception mode, characteristic that allows to get the reflectivity at horizontal polarization (henceforth called Z for simplicity), differential reflectivity Z_{dr}, the differential phase φ_{dp}, among other variables. The gates resolution is 200 m, with a total covered range of 100 km. The raw radar dataset was processed to reduce the influence of the attenuation observed at X-band frequencies and to present better Z_{dr} estimates. To do so, the radar performed a zenith-pointed scan (also known as a “bird-bath” scan) after each volume scan. The Z_{dr} offset trend observed during time can be then corrected. To derive K_{dp} the φ_{dp} was filtered and smoothed using a FIR (finite impulse response) filter and then the K_{dp} is estimated by deriving the smoothed φ_{dp} curve (Hubbert & Bringi, 1995). Attenuation correction was applied to both Z and Z_{dr} using the ZPHI method proposed by Testud et al. (2000).

From the processed radar data, we calculate Z CAPPIs (Constant Altitude Plan Position Indicator) every 500 m, from 2 km up to 18.5 km. The CAPPIs have 1 km resolution, with the radar at the center of the grid (22° 48’ 50’’ S, 47° 3’ 22’’ W). The volumetric data is interpolated to the CAPPI grid by using a weighting function based on the distance between volumetric and CAPPI pixels. In that way, the CAPPI grid points can be affected by multiple volumetric pixels, with weight inversely proportional to their distance.

2.2 ForTraCC

In order to automatically track precipitating clouds, we employed the ForTraCC (Forecasting and tracking Cloud Clusters – Vila et al., 2008) system. This algorithm was initially developed to detect and track cloud clusters from GOES imagery but was later adapted to work with radar CAPPIs by Queiroz (2009). In this study, we locate and track rain cells on CAPPIs at 2 km height (1 km horizontal resolution). ForTraCC is able to track rain cells by applying a minimum threshold in rain rate (R) or Z. Here we use the threshold of R = 5 mm h^{-1} to identify the cells, which is equivalent to around 34 dBZ according to the Marshall-Palmer Z-R relation. This is a relatively high threshold as compared to the more usual 20 dBZ limit. The intent is to avoid too much chaotic mergers and splits and to reduce the noise in the overall statistics due to high numbers of small rain cells. The result is that we effectively detect more mature rain cells than usual, but their lifecycles are more clearly defined. Rain cells detected with our methodology must present an area of at least 10 pixels (or 10 km^2) to be tracked and mergers and splits are tracked according to the maximum overlap area between sequential CAPPIs. Because rain cells must conform to the threshold throughout the lifecycle, the 34 dBZ limit also means the latter stages are not fully captured. However, the most intense stages of the cells are likely better represented compared to a noisier 20 dBZ threshold.

CAPPIs are calculated every 10 minutes, enabling ForTraCC to store physical and morphological characteristics of the rain cells throughout their lifecycle. Such characteristics include cell’s area evolution, movement speed and direction, among others. Therefore, ForTraCC allows the definition of a Lagrangean dataset with rain cells characteristics. The specific parameters obtained in this work are listed below.

Every rain cell identified is treated as a 3D cylinder, where its horizontal radius (r, in km) is obtained from the cell area (A, in km^2) provided by ForTraCC:

$$r = \sqrt{\frac{A}{\pi}} + 2 \quad (1)$$

Where 2 km are added to r to compensate for possible vertical tilting of the clouds. By using the same r in every altitude level, the cylinder is defined and it follows the cells throughout their lifecycle.

The cylinders are used to obtain Lagrangean properties of the rain cells from the CAPPIs as well as the volume scans. The properties calculated are separated between macro- and microscale as listed below. Macroscopic characteristics obtained are:

a. Maximum area A_{max} (at 2 km), calculated as the maximum A in the cell lifecycle.

b. Duration ΔT (in minutes), calculated by $10(n-1)$ where n is the number of CAPPIs in the cells lifecycle.

c. VIL (Vertically Integrated Liquid, in kg m^{-2}), calculated by:

$$VIL = \sum_{i=1}^{34} 3{,}44 \cdot 10^{-6}[(Z_i + Z_{i+1})/2]^{4/7} \cdot \Delta h \tag{2}$$

where i represents each of the 34 CAPPIs between 2 km and 18.5 km altitude and Δh = 500 m. In order to minimize possible melting hail effects, we truncate horizontal reflectivity in 57 dbZ such that $Z(Z > 57\ dBZ) = 57\ dBZ$. This calculation treats all column as liquid water for simplicity. Because convective clouds often present supercooled droplets, the separation between liquid and frozen hydrometeors can be very complex. Therefore, the VIL values reported here can be understood as an overall indication of the rain cells water mass rather than precise retrievals.

d. System top altitude (H_{top}, in km), calculated as the maximum echo top of 20 dBZ in the cylinder in each time step. Note that while the 34 dBZ threshold is enforced on the 2 km CAPPI for tracking purposes, the other levels do not have similar restrictions and only follow the evolution of the tracked rain cell at 2 km altitude.

e. VIL density (DVIL), calculated as the ratio between VIL and echo top of 20 dBZ.

f. Total water (W_T, in t), calculated by the areal integration of VIL.

Within every cell cylinder, the altitude level with the highest amount of water mass was looked for in a similar way as in Heiblum et al. (2016a,b), Chen et al. (2017) and Dagan et al. (2018). Those studies reduce the analysis of whole clouds to their COG. However, here a slightly different approach was adopted in which we do not directly calculate the mass-weighted average altitude. Instead, we define a center of activity (COA) as the altitude level that most contribute to the system average VIL. This level is somewhat similar to COG, but is much more adequate for radar applications, especially for operational applications. Because there is no mass-weighing of all altitudes, its calculation is much simplified. As will be shown later, the vast majority of the COA data is contained within the lower 4.5 km CAPPIs meaning that it is primarily related to liquid droplets for the region. The pair of COA and VIL will be used here to characterize the rain cells macroscale properties.

Formally, COA is calculated from (3) without the altitude integration. In this way, we have each CAPPI's contribution to the total VIL:

$$VIL_i = 3{,}44 \cdot 10^{-6}(Z_i)^{4/7} \tag{3}$$

By averaging VIL_i for every CAPPI (i.e. every i), we define the average vertical profile of the contributions to VIL. COA is obtained as the altitude of the level with the highest contribution.

For the microphysical approach, in this study we will focus on polarimetric variables and Gamma DSD parameters estimated from them. Because the DSD retrieval is an under constrained problem for radar applications, it is unfeasible to construct a full Gamma phase space as in Cecchini et al. (2017). Instead, the intent is to study DSD parameters values in the macroscale context provided by COA and VIL. We obtain the DSDs directly from the volume scans instead of the CAPPIs because Z_{dr} and K_{dp} values are also needed.

The Gamma DSD is estimated from the volumetric fields of Z, Z_{dr} and K_{dp} following Kalogiros et al. (2013). The authors show a method to obtain the normalized gamma DSD, which has the form:

$$N(D) = N_w f(\mu) \left(\frac{D}{D_0}\right)^{\mu} \exp\left[-(\mu + 3{,}67)\frac{D}{D_0}\right] \quad (4)$$

where N_w is the intercept, D_0 is the mean volumetric diameter and μ is the shape parameter. The function $f(\mu)$ is given by:

$$f(\mu) = \frac{6}{3.67^4}\frac{(3.67+\mu)^{\mu+4}}{\Gamma(\mu+4)} \quad (5)$$

The advantage of the Kalogiros et al. (2013) method is that it was specifically designed to work with X-band radars, where Mie effects are significant. However, because there are three parameters to estimate with only two DSD moments detected by the radar, the problem is under constrained and an assumption has to be made about the relation between droplets size and DSD shape. To constrain the equations, Kalogiros et al. (2013) propose the following μ-D_0 relation:

$$\mu = 165e^{-2.56D_0} - 1 \quad (6)$$

For more details on the DSD retrieval methodology see Kalogiros et al. (2013). In this study we will use the normalized gamma format because it more suitable to radar applications. However, it is important to point out that the normalized gamma in Equation 4 can be easily converted to the Gamma format introduced by Ulbrich (1983) that is used in Cecchini et al. (2017) by:

$$N_0 = N_w f(\mu) D_0^{-\mu} \quad (7)$$

$$\Lambda = \frac{\mu+3.67}{D_0} \quad (8)$$

2.3 Analysis period and rain cells selection

The results presented here are focused on the 2016/2017 summer, more specifically between November 22nd, 2016 and March 3rd, 2017. Within this period, 21 days were chosen for analysis, based on data availability and occurrence of precipitation. While ForTraCC detects rain cells throughout all radar range (100 km), we will focus exclusively on those that had their entire lifecycle within 10 km to 60 km from the radar. Additionally, cells were manually and qualitatively filtered based on PPI coverage and overall precipitation type. Cases associated with small numbers of PPIs, either relatively shallow clouds or cells close to the 60 km circle that have only a few cross-sections in the volume scan (e.g. 3 or less), or cases immersed in stratiform systems (qualitatively analyzed case by case), were excluded. With those filters, 446 cells remained for analysis.

An example of the tracking algorithm functioning is shown in Figure 1. The rain cell was a relatively shallow precipitating cloud that was detected in November 26th, 2016 at 19:00 UTC (16:00 local time) and lasted approximately 20 minutes. The cell evolution is shown in the 2km CAPPIs in Figures 1a-c, while the respective volume scans inside the cylinder discussed in the previous section are shown in Figures 1d-f (limited to $Z \geq 30$ dBZ for clarity). Note that this strategy allows not only the study of the evolution of macroscopic characteristics such as the cell area and depth, but also its internal structure in a Lagrangean way. Applying the same methodology to all rain cells detected by ForTraCC allowed the creation of the object-oriented dataset that will be discussed here.

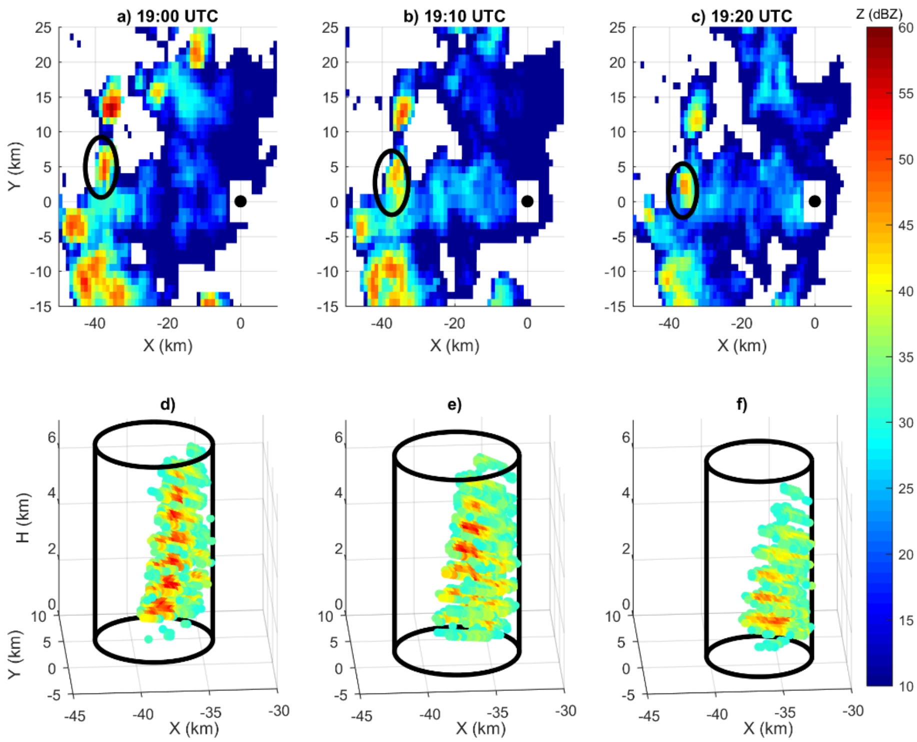

Figure 1: example of the tracking algorithm functioning. This rain cell was detected on November 26th, 2016 at 19:00 UTC (16:00 local time) and lasted approximately 20 minutes. Graphs in a-c are the 2-km-height CAPPI evolution of the cell (highlighted by the black circles), as detected by the methodology described in this section. The black dot at {0, 0} is the radar. Graphs in d-f are the respective evolution of the PPIs in the volume scan, where only $Z \geq 30$ dBZ points are plotted. In all graphs X and Y represent east and west distances from the radar, respectively, and H is the altitude.

3 Results

3.1 Overall rain cells characteristics

The rain cells detected by the X-band radar throughout the analysis period present high variability in terms of morphological aspects. While around 55% presented duration and area of 20 minutes and 40 km^2 or less, respectively, there were also cells that lasted for more than one hour that covered a few hundred km^2 (Figure 2). Rain cells maximum area and duration are usually correlated, as found by previous studies in several regions (e.g. Machado & Laurent 2004 for the Amazon). The same was found here (not shown), where the larger rain cells took longer to dissipate.

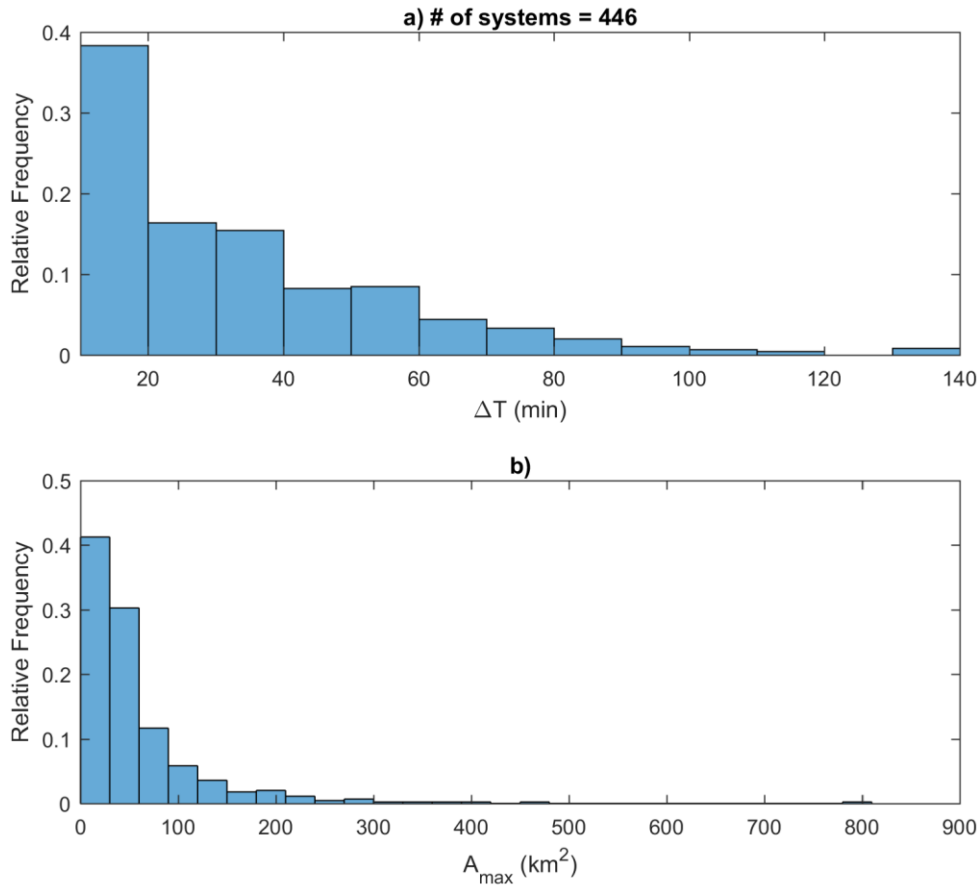

Figure 2: normalized histograms of a) duration ΔT and b) maximum area Amax by the cells detected by ForTraCC. Note that the minimum values in the vertical bars are inclusive, so a bar between 10 min and 20 min is associated to the former and so on. The same is valid for the maximum area histogram in b).

In terms of the diurnal cycle of rain cells, we found two main peaks of activity: one at the afternoon/late afternoon and another at late night/early morning. It is likely that a significant amount of rain cells in the afternoon are linked to local convection, while events in the night/early morning are possibly associated to larger-scale systems. Even though we do not apply a classification criterion, it should be noted that the overall statistics shown here are largely representative of afternoon short-lived systems because of their larger sample size (70% of the macroscale data is within the 16:00 UTC to 22:00 UTC period, which is between 13:00 and 19:00 local time).

One of the main interests of this study is to analyze the property COA and how it relates to the other characteristics of the rain cells. Figure 3 shows the relation of COA to W_T, H_{top}, VIL and DVIL. Firstly, we note the limitation of 500-m-resolution in the COA calculation, because of the vertical interval between the CAPPIs. Additionally, 97% of the data present COA equal to or lower than 4.5 km and that is why apply this limit to the figure. It also means that COA is usually below the 0 °C level (around 4.5 km or higher for the region). This is a result not only of the water mass accumulation on those levels but also of the different ways liquid droplets and ice particles interact with radiation. Because of the oblate shape and higher dielectric constant, the horizontal reflectivity of raindrops is higher than that of ice particles with similar sizes. Additionally, the melting of ice results in higher reflectivity close to the 0 °C level and below. Those factors further favor the limitation of COA to heights up to 4.5. With that said, it is possible to note a positive relation between COA and W_T (Figure 3a), H_{top} (Figure 3b), VIL (Figure 3c) and DVIL (Figure 3d) in terms of the median behavior. It shows that higher COA is generally related to deeper cells with high amounts of water inside. Even though COA is related to the median W_T, H_{top}, VIL and DVIL, Figure 3 shows that there is a lot of variability as well. It is possible to see the significant overlap between the interquartile ranges of different COA values (blue bars in Figure 3). This is a result of varying rain cells characteristics such as their sizes, the underlying thermodynamic environment they are embedded in and different life cycles that may or may not include mergers and splits. Additionally, it highlights that COA is a characteristic that is shared among significantly different rain cells. For instance, the interquartile range shown in Figure 3c indicates that rain cells with COA = 4.5 km have VIL between 2 kg m^{-2} and 4 kg m^{-2}. While those types of cells present significantly different quantities of water and different intensities overall, they likely share similar vertical structure. Therefore, by combining a measure of the cells overall amount of water with COA may prove invaluable to holistically understand the rain cells appearance and life cycle.

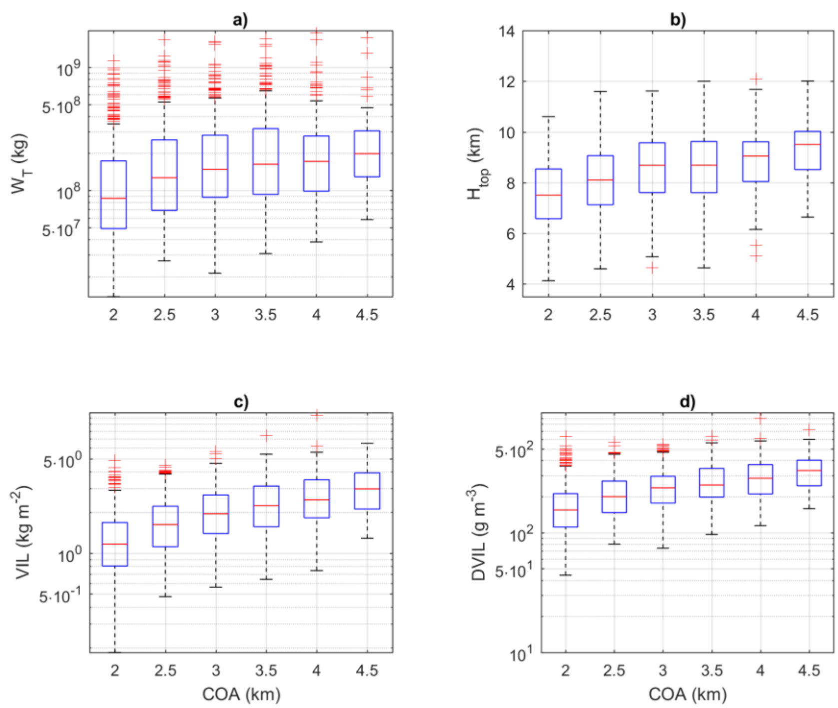

Figure 3: boxplots of a) WT, b) Htop, c) VIL and d) DVIL as function of COA.

The simulations shown in Heiblum et al. (2016a) show that the rain center of gravity is at the same altitude as the cloud center of gravity when a new convective cloud is formed. When the cloud grows and start producing more rain droplets, their center of gravity gets higher than that of cloud droplets. The situation is reversed by the onset of precipitation. Given that all rain cells must start as shallow cumulus, a similar pattern is expected for COA. However, as discussed earlier, our methodology detects rain cells already at a relatively mature stage. Therefore, it is reasonable to expect that COA is high at the cell detection and then it sinks following the precipitation and dissipation processes. To confirm that, we calculated the rain cells percent time such that 0% corresponds to the detection and 100% to the dissipation. By averaging this time according to the cells COA, we obtained the results shown in Figure 4. We note that the 0% and 100% limits here are limited by the ForTraCC threshold chosen and are not related to the visual aspect of the clouds. Because the threshold is relatively high (34 dBZ), the results within 0% and 100% percent time cover basically the early to late mature phase. The growing and dissipation stages are likely underrepresented in our results.

If the ForTraCC threshold was reduced, it would likely be possible the detection of rain cells in earlier and later stages of their life cycle. However, as discussed in Section 2.2, this would also add noise to the statistics by including several smaller systems that have relatively limited precipitation capabilities and that present chaotic merger and splits events. On the other hand, high thresholds such as the one used here provide better statistics for the fewer systems detected. In this study, we chose to stick to the high threshold in order to calculate rain cell statistics without requiring too much data filtering. The downside is that the systems are detected already close to maturation and there is not much information on the growing or dissipation stage. Nevertheless, the characterization of the early and late mature stages shown here may help nowcasting techniques by providing the benchmark of where the relatively intense systems grow to. For future case studies, or even operational implementation, a lower threshold may be considered if additional filters are put in place.

Figure 4 confirms that the median behavior of the rain cells is to present COA around 4 km or 4.5 km early on, which decays with further cell evolution. Of course, there is a lot of variability as well due to the complexities of the rain cells dynamics and the limitations of the measurement setup. Firstly, we note that different rain cells may present different COA motions according to their thermodynamics. For instance, cells that are able to sustain strong updrafts may support higher COA for longer periods of time. On the other hand, cells with high precipitation efficiency can have rapidly sinking COA. Additionally, the 10 minutes limitation of the CAPPIs means that the cells may be captured at slightly different stages of their relative life cycle.

In order to further understand the role of COA, it is important to analyze the cell characteristics discriminating by its value. Figure 5 presents reflectivity contoured frequency by altitude diagram (CFAD, Yuter & Houze, 1995) plot for Z > 10 dBZ when the cells present COA between 2 km and 4.5 km. Here we note that, while ForTraCC was set up to work with a 34 dBZ threshold, lower reflectivity values are contained in the rain cells cylinders (as in Figure 1) for two reasons. Firstly, the 34 dBZ limit is only enforced for the 2 km CAPPI, so lower Z can appear in higher levels. Additionally, the added 2 km in the rain cells radii described in Equation 1 means that lower Z values are allowed inside rain cells even at the 2 km altitude level. The CFADs in Figure 5 were obtained from the CAPPIs, with H and Z intervals of 0.5 km and 2.5 dBZ, respectively. The number of data in each bin is represented in colors, while the dashed black lines are averaged Z profiles. The horizontal lines represent the respective COA value for clarity. This figure clearly shows that COA has a strong relation to the overall appearance of the rain cells. Note that all graphs in Figure 5 show a boomerang-like shape (except Figure 5f where it is cutoff) with COA at the middle. It shows that the cells usually have the appearance of

Figures 5a,b when they are detected and then evolve along the sinking COA (Figures 5c-f), taking into account the results shown in Figure 4.

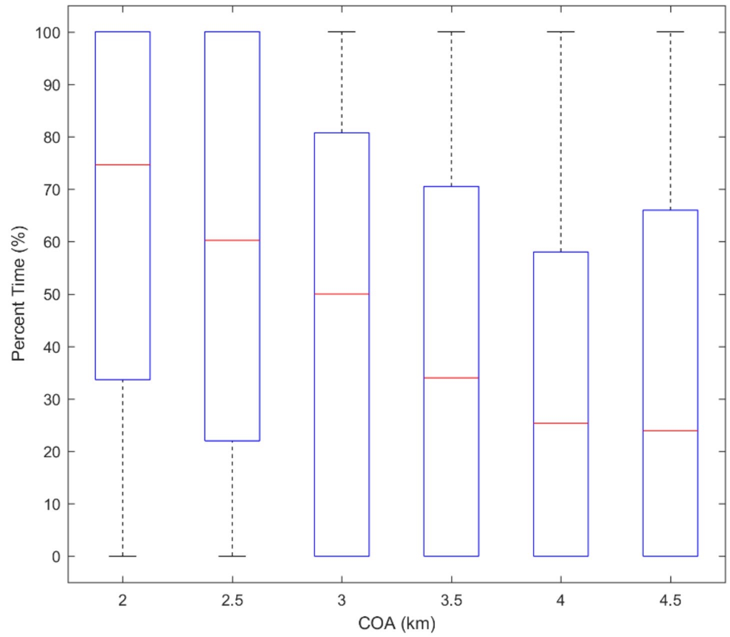

Figure 4: boxplot of percent time as function of COA. Percent time is 0% on system formation and 100% on dissipation according to the ForTraCC criteria chosen.

The boomerang-like shape can be mostly explained by a few competing processes. For high COA (e.g. ≥ 3.5 km), the decrease of Z with altitude is characteristic of growing ice-to-liquid ratios. The higher the relative amount of ice, the lower the reflectivity will be. For lower COA, the decrease in Z is related not only to the ice-to-liquid ratio but also to the overall rain cell collapse. Below COA, the Z decrease towards the surface is most likely associated to evaporation. However, collection processes also take place in regions close and below the COA. Because COA is associated to the highest reflectivity values, it means that collection processes, together with ice melting, dominate in the COA layer.

As mentioned earlier, there is significant variability of reflectivity values and consequently water mass for systems sharing the same COA. Therefore, despite having different absolute values, it is possible to conclude that COA captures one fundamental aspect of the rain cells. But it is noteworthy that the variability of Z around COA is similar for all values of the latter. Around COA the reflectivity values tend to vary between 30 dBZ to 45 dBZ in terms of the most common rain cells observed here. Additionally, the averaged Z at COA varies only roughly 2 dBZ, going from 44.5 dBZ in Figure 5a down to 42.6 dBZ in Figure 5f and decaying almost linearly with COA. This indicates that COA is a layer in relative balance not only in the vertical but also throughout the rain cells life cycles. Below COA, the averaged profiles are within a range of 3.7 dBZ and this difference tends to grow with altitude. For instance, above 8 km the maximum difference between the averaged profiles reach 29.4 dBZ due to high reflectivity for 3.5 km ≤ COA ≤ 4.5 km and low reflectivity for 2.0 km ≤ COA ≤ 3.0 km. This shows that higher COA are associated to more active ice phase given the likely higher water mass available at high altitudes. It is also likely that high COA are related to Z_{dr} columns.

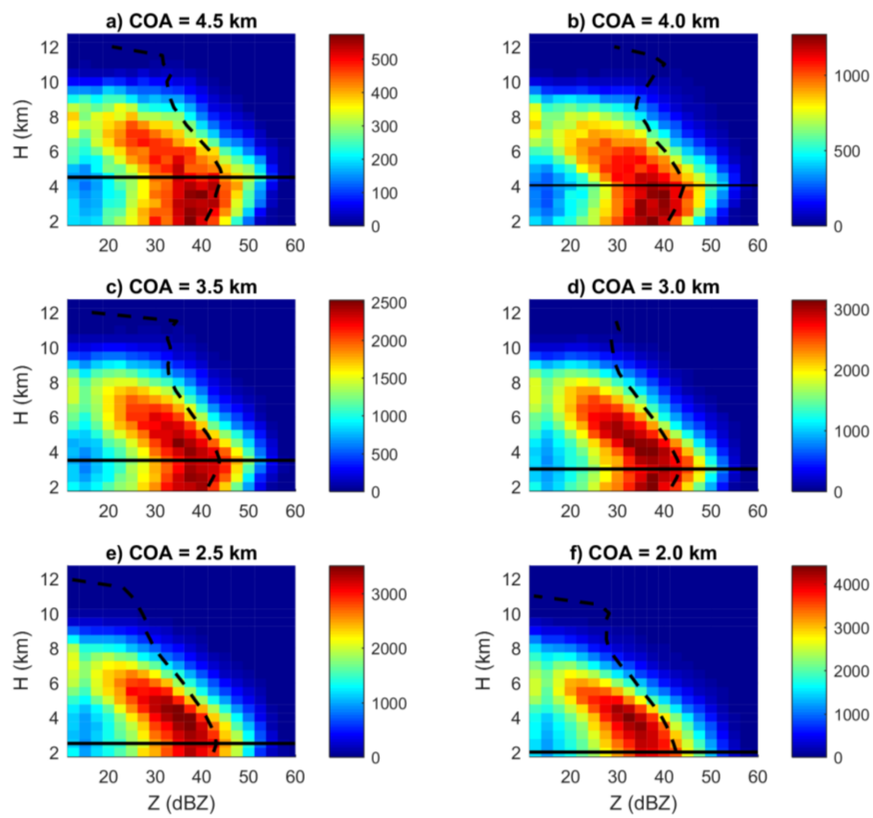

Figure 5: reflectivity CFADs discriminated by COA. The continuous black lines represent COA for clarity, while the dashed black lines represent averaged Z profiles for the same data (calculated on linear scale before converting back to dBZ). The number of points in each H and Z bins are shown in colors.

While Figure 5 paints a cohesive view of the rain cells, it lacks representation of individual systems that may have different COA physics. For instance, short- and long-lived cells can present contrasting COA characteristics because the dynamic and thermodynamic processes sustaining them is different. In order to address this issue, we present the results in a similar way to Heiblum et al. (2016a) in Figure 6. The intent of this calculation is to obtain the average behavior of cells sharing similar durations. Because each system may have different characteristics at detection, a normalization process is used. The evolutions shown in Figure 6 are all relative to the properties observed at detection (identified with a 0 subscript). Because of the normalization, all trajectories start at the (1,1) point, indicated by the junction of the two dashed black lines. From this point on, the trajectories are calculated for the same 10-minute time step of the cells sharing the same duration – 10-minutes cells have two points, 20-minutes cells present three points and so on. Every trajectory represents averaged values between cells of the same duration, whereas cells with mergers and/or splits detected by ForTraCC were excluded.

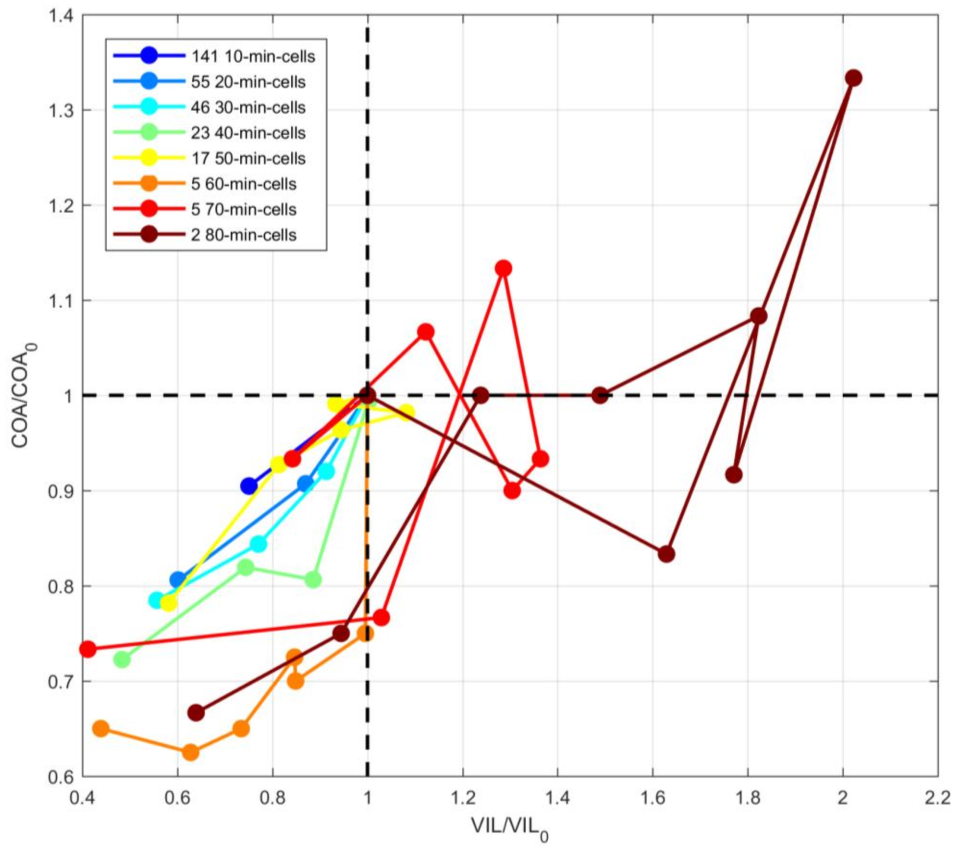

Figure 6: trajectories in the normalized phase-space COA-VIL. Both COA and VIL are normalized by their values at system detection (COA_0 and VIL_0, indicated by black dashed lines) to compensate for possible different initial conditions. All trajectories start at the (1,1) point and evolve from there. The number and duration of the systems is given in the legend.

Figure 6 shows that cells lasting up to 60 minutes have a similar pattern in the COA-VIL phase space. From the starting point, they evolve towards the third quadrant, where both COA and VIL diminish over time. The difference between their trajectories is mainly on how they evolve in this quadrant. Except for the yellow line (50-minutes cells), there is a trend of increasing curvature from short- to long-lived cells. In other words, short-lived cells tend to lose COA and VIL in a similar proportion, whereas longer-lived ones may retain some VIL even while COA sinks. This can either mean that longer-lived cells usually start with higher COA or that the layer around their COA contain relatively more water that remains in the cloud when the bottom part precipitates. Even though there is a lack of a significant sample size for cells lasting 70 minutes or more (with no merger and/or split), it is notable that they were the only ones that meaningfully evolved through the right quadrants. Those quadrants exemplify processes in which the rain cells gain mass with either ascending or descending COA. Therefore, longer-lived cells present some sustained source of water mass even after it reached the relatively mature stage as detected by our methodology. This could be either microphysical mechanisms, such as continued droplet growth by sustained updrafts or melting ice falling from above, or some form of dynamical feedback. Either way, a case-by-case analysis would be ideal to elucidate such aspects.

Given that the COA is a layer of interest because of its relation to rain cell life cycle and internal structure, it is important to analyze its microphysical properties to provide a reference for the comparison of individual cases. Figures 7 and 8 show median polarimetric variables and associated DSD parameters taking into account the macro characteristics of the cells (COA and VIL). Every point represents median properties from volume scans in 1-km vertical layers around COA and for every 1 kg m^{-2} VIL interval (see figure description for more details), for the same cells as in Figure 6. Basically, it represents a snapshot of the most intense region within the COA level.

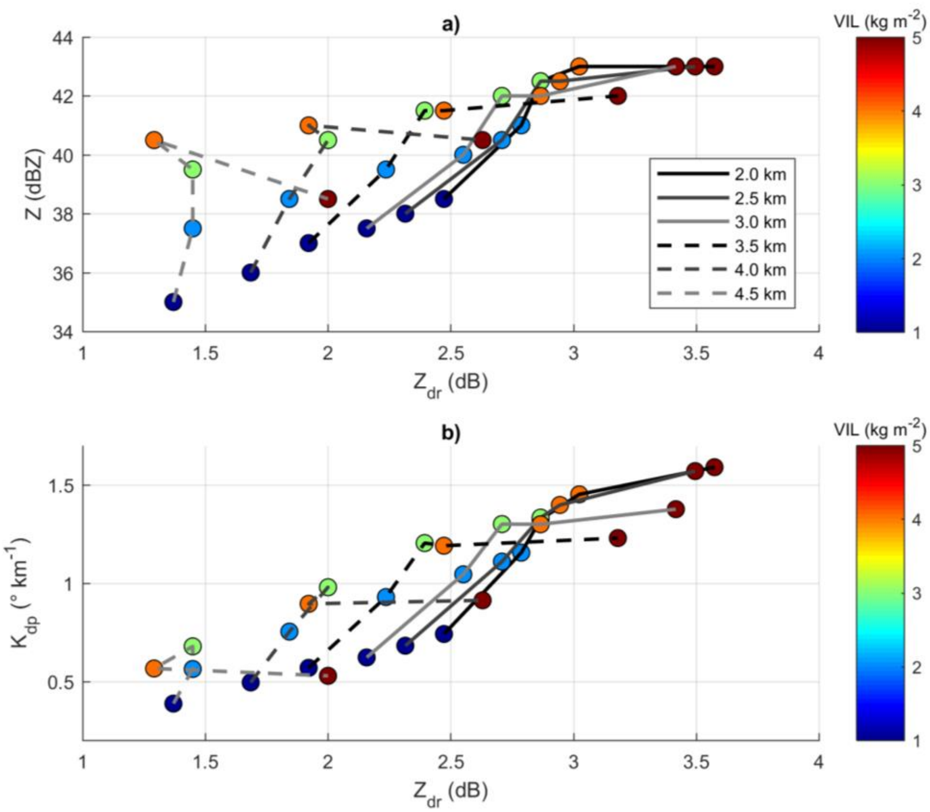

Figure 7: median polarimetric variables as function of COA and VIL. While VIL and COA were obtained from the CAPPIs, Z, Zdr and Kdp are from the volume scans, limited by the following thresholds: 1) Z > 30 dBZ; 2) Zdr > 0.5 db; 3) Kdp > 0 ° km-1; 4) ρHV > 0.97; 5) elevation angle α ≤ 15 ° and 6) COA – 0.5 km ≤ H ≤ COA + 0.5 km. Those thresholds aim to focus the analysis primarily on the cell core at the 1 km layer around COA. The rain cells considered here are the same as in Figure 6, where no merger or split was automatically detected. VIL values are represented by circle colors, showing the upper bound of every 1 kg m-2 interval. For instance, dark blue points are shown as VIL = 1 kg m-2 and are related to the interval 0 kg m-1 < VIL ≤ 1 kg m-2. The different curves represent medians of all volume scan measurements that follow the criteria above while the cell presented the specified COA (legend in Figure 7a). The Z and Zdr medians were obtained directly in dB scale. The average number of data for each point is 23366, going from a minimum of 2387 to a maximum of 71837.

Figure 7 shows the evolution of Z, Z_{dr} and K_{dp} according to COA and VIL individually, as well as a combination between them. While an increase of the polarimetric variables with VIL is expected, it is somewhat counter-intuitive that they also increase with decreasing COA because of rain cell dissipation. As they approach 2 km in altitude, the cells are closer to being dissipated but their inner core have reached peak values of the polarimetric variables. However, it is important to highlight that this will only happen in case VIL remains relatively constant. In individual rain cells, both COA and VIL can diminish during dissipation (Figure 6) and the overall polarimetric characteristics will largely depend upon their balance.

Another interesting pattern in Figure 7 is the capping in Z and K_{dp} values for high VIL. For fixed COA levels, Z and K_{dp} tend to grow proportionally to Z_{dr} up to VIL = 3 kg m^{-2}. From this point on, Z_{dr} continues to grow while both Z and K_{dp} either stagnate or increase ever so slightly (Z even decreases from VIL = 4 kg m^{-2} to VIL = 5 kg m^{-2} for COA = 4.5 km and COA = 4.0 km). This indicates that high VIL cells present different microphysical characteristics in its center of gravity. Those cells have both bigger droplets overall (Figure 8) and larger amounts of water for the sinking-COA-droplets to collect, further favoring their growth. However, possible attenuation of the radar signals can also help explain the capping – especially in Z.

From the results shown in Figure 7, the corresponding normalized gamma DSD parameters were obtained by applying the method described in Kalogiros et al. (2013). This method was developed to correct for Mie effects specifically for the X-band range and the results are shown in Figure 8. Firstly, we note that the mirroring between Figure 8a and Figure 8b is explained by the μ-D_0 constrain in Equation 6. Nonetheless, the range of μ values provided can be used to further characterize the cells COA microphysical properties. Following the patterns in Figure 7, D_0 also tends to increase with increasing VIL and decreasing COA. However, this is not followed by a monotonic variation in N_w. Note that this parameter tends to grow from VIL = 1 kg m^{-2} up to VIL = 3 kg m^{-2} and then decreases with increasing VIL. When both N_w and D_0 increase, the overall number of droplets of the DSD increases unevenly in terms of contribution to the total water mass. In other words, D_0 increases by an increase of the number of relatively big droplets even when smaller droplets are also more numerous. On the other hand, lower N_w with bigger D_0 indicate that there are less droplets on both ends, but the smaller ones contribute even less to the DSD water mass. That difference may be explained by the increased efficiency of the collection process on high VIL cases, where a turning point is around VIL = 3 kg m^{-2}. This turning point approximately coincides with the Z and K_{dp} capping shown in Figure 7.

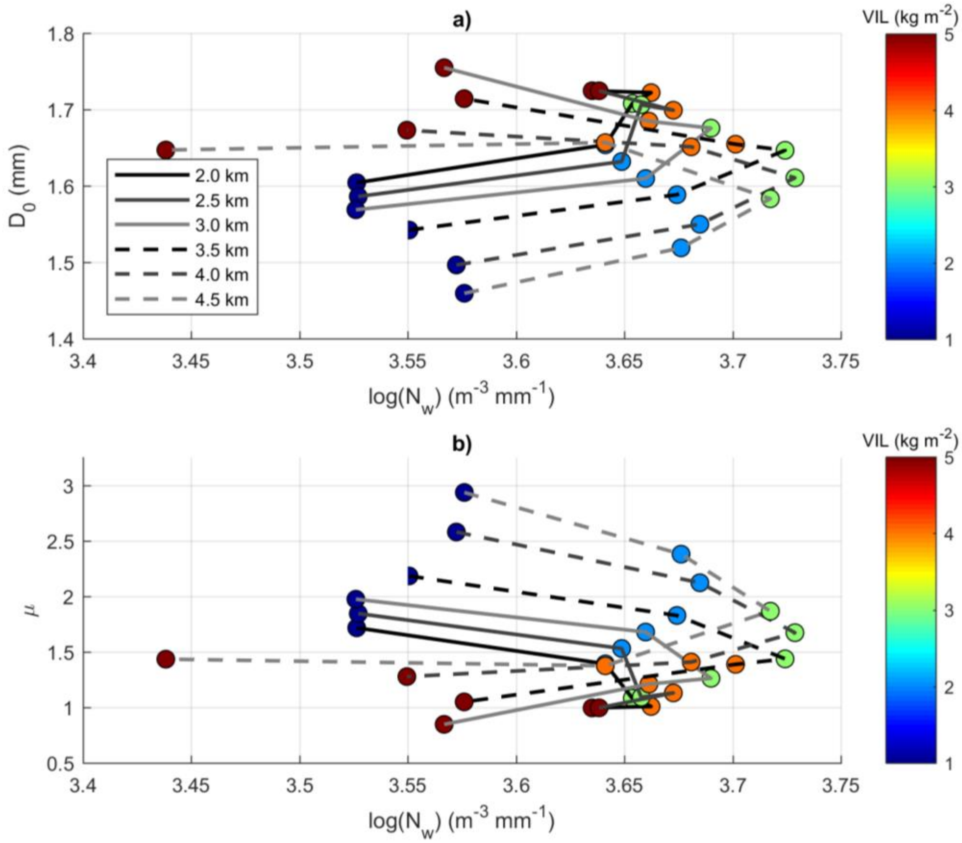

Figure 8: same as Figure 7 but for the DSD parameters obtained by the respective medians of Z, Zdr and Kdp using the method described in Kalogiros et al. (2013). Nw is shown in log-scale (base 10) for simplicity.

3.2 Case studies

Two case studies were selected to exemplify physical characteristics of individual rain cells as seen by the COA/VIL approach. The cells were selected not based on their particular intensity, but rather to exemplify how different COA characteristics are related to the overall cells appearance. We chose two rain cells during November 28th, 2016, with overall properties shown in Table 1. For the case studies selection, we allowed merger and splits occasions because it was possible to analyze them in more detail.

Table 1: overall characteristics of the case studies. *Calculated as the sum of accumulated rainfall in every 2-km-CAPPI pixel with Z > 10 dBZ using the Marshall-Palmer Z-R relation and assuming that each pixel remained static (Z = constant) for the 10-minute intervals.

Case # and time steps (UTC)	**COA (km)**	**VIL (km m^{-2})**	**H_{top} (km)**	**New/Split/Merger/ Continuity**	**Total Accumulated Rainfall* (mm)**	**A (km^2)**
Case 1						
17:40	4.5	6.49	9.0	New	78	14
17:50	3.5	2.49	8.6	Continuity	267	41
18:00	4.0	2.08	9.0	Continuity	404	36
18:10	3.5	3.41	9.5	Merger	763	133
18:20	3.5	2.60	9.1	Continuity	1014	85
18:30	3.5	1.76	9.1	Split	1131	34
Case 2						
18:50	4.5	2.41	6.6	New	73	18
19:00	2.5	2.13	7.0	Continuity	209	22
19:10	2.0	1.04	7.0	Continuity	302	26
19:20	2.0	0.74	7.0	Merger	350	19
19:30	2.0	0.86	7.0	Continuity	413	20
19:40	2.0	0.66	7.1	Continuity	480	27

From Table 1, we note that the rain cells followed the overall trend of high COA upon detection. However, we chose two cases with different COA trends. Note that Case 1 presents relatively high COA throughout its lifecycle, which ends in a split (the resulting cells from the split did not meet the ForTrACC requirements to be tracked). On the other hand, Case 2 present a rapidly decaying COA. Both cases presented merger occasions automatically detected by ForTraCC. The merger in Case 1 was followed by an increase in VIL, A and H_{top}, but the same was not observed for Case 2. This could be a reflection of the different convective environment for the two cases, illustrating the complexities of the dynamics involved. From Table 1 it is clear that Case 1 is the stronger one, with more than double the total accumulated rainfall of Case 2.

For each case study selected, the cells cores were looked for based on polarimetric variables thresholds. For every radar elevation angle, we have a respective cross-section (slice) of the rain cells. In each of those slices, the core is found by: 1) $Z \geq Z_{0.75}$ for altitudes below 4.5 km, where $Z_{0.75}$ is the 75% percentile of Z in the slice and 2) $Z \geq 10$ dBZ, $Z_{dr} \geq 1.0$ dB and $\rho_{HV} \geq 0.85$ for altitudes above 4.5 km and below 8 km (based on the Z_{dr} column criteria of Carlin et al., 2017). The 4.5 km altitude is an approximation for the 0 °C isotherm level. Given that we are analyzing only a few cases in more detail and that criteria 1 and 2 perform similarly for liquid-dominated volumes, there was no need for precise measurements of 0 °C isotherm altitude and the value is close to average radiosonde measurements. For the two criteria, we further enforced horizontal consistency as in Carlin et al. (2017), where every 9x9 range-azimuth pixel box was required to have at least 5 pixels meeting requirements 1 or 2. Overall, the criteria aim to find the most active portion of the systems along radar rays and where liquid droplets predominate.

Figure 9 shows the evolution of vertical profiles of polarimetric variables for the case studies, where each point represents averaged properties based on the criteria mentioned above. We chose to use averages instead of medians (as in Figure 7) because there were no rigid spatial criteria, i.e. we do not calculate averaged properties inside a specific cartesian volume. Additionally, because we are now treating each cell individually, the overall distances from the radar are similar and so are the illumination volumes of each pixel considered (which is not the case in Figure 7, where different cells are considered). In that way, all pixels are considered to have the same weight to the average in a reasonable approximation. For both Z and Z_{dr}, the averages were taken in linear scale and then converted back to dBZ and dB, respectively.

The rain cells usually start off with the highest Z and Z_{dr} values overall (Figure 9), which then decays as COA sediments. The rate in which Z diminishes is higher in the upper parts of the systems (e.g. above 5 km) as COA moves away from those layers. It is interesting to note that peak K_{dp} values in the lower levels occur 10 minutes after the peak in Z_{dr} at system detection. This might be explained by the different balance between droplets mean size and their overall number concentration. Peak Z_{dr} values are associated to peak D_0, but there are relatively few droplets as seen by low N_w values. This illustrates the process in which the biggest droplets reach the ground faster given their higher terminal velocity and are then followed by the bulk of the precipitation. Indeed, Table 1 shows that the total accumulated rainfall increases by a factor of 2.9 (Case 2) and 3.4 (Case 1) from the first to the second time steps of the cells, which is the highest increase during their lifecycle. Of course, this increase is due not only to increased precipitation rates but also to increased covered area at 2 km altitude. Additionally, a portion of the K_{dp} peak can be explained by the melting of ice as the upper layers start to collapse, which should also decrease Z_{dr}.

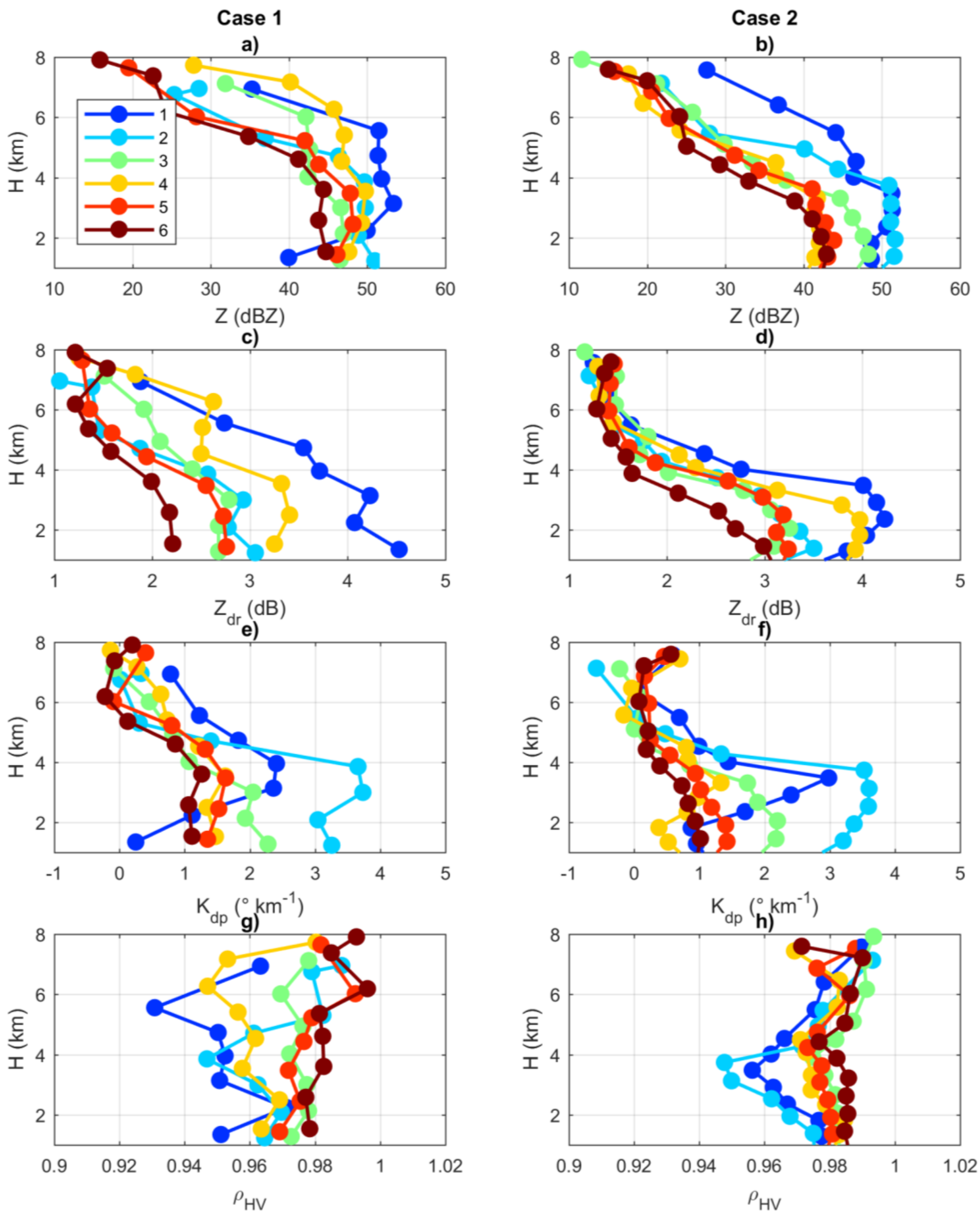

Figure 9: averaged vertical profiles of polarimetric variables for Case 1 (left column) and Case 2 (right column). Each datapoint represents the average of a single slice of the system, according to the criteria mentioned in the text. The legend specifies the time-steps of each case in chronological order (same number of time steps for both cases, where the specific UTC times are given in Table 1).

Averaged ρ_{HV} profiles are provided in Figure 9 as a general indication of the level of hydrometeor mixture in the rain cells cores. We note that ρ_{HV} starts lower at cell detection throughout the core, suggesting higher levels of mixture, and then converges to higher values (around 0.98) for later stages of the lifecycle. This shows that when the cells are detected it is more likely to find both ice particles below and liquid droplets above the 4.5 km altitude mark. Also noteworthy is that the values are much higher than the limit of 0.85 imposed in the filters. The overall appearance of the ρ_{HV} profile presents correlations with the systems macroscale characteristics. Note that Case 2 have much smoother ρ_{HV} profiles as compared to Case 1 with lower values contained in the region between 2.0 km and 4.0 km. This pattern is followed by a characteristic variation of Z_{dr} where it quickly decays with both time and altitude above the 3 km mark. Both mechanisms are related to the relatively quick sedimentation of COA. As shown in Table 1, Case 1 have COA at 2.5 km already at the second time step, limiting its ability to mix ice and liquid hydrometeors and consequently to generate a strong (or large) Z_{dr} column. On the other hand, Case 1 maintain relatively high COA for a longer period of time which is accompanied by higher Z and Z_{dr} (and even K_{dp}) above 4.5 km altitude. This indicates that COA may be a good indicator of Z_{dr} columns in continental systems, especially when paired with VIL estimates or Z profiles. Additionally, Lier-Walqui et al. (2016) show that positive K_{dp} values above the melting level is usually associated to updrafts meaning that this is likely one of the key mechanisms to sustain high COA in Case 1. If high COA is considered to be a proxy for both updrafts and Z_{dr} columns, this could be an important contribution for operational purposes given that the identification of COA does no rely on polarimetric retrievals.

The polarimetric profiles for Case 1 resemble profiles of highly electrically active systems shown in Mattos et al. (2016), where they present high Z, Z_{dr} and K_{dp} with low ρ_{HV} in the low levels. At higher levels, those systems have slightly positive K_{dp} and Z_{dr} accompanied by $Z >$ 30 dBZ. This kind of values were observed for Case 1 for several time steps in the beginning of the life cycle captured by our methodology. At later stages of development, Z falls below the 30 dBZ threshold above 4.5 km, which is followed by a decrease in K_{dp}. According to Mattos et al. (2017), positive K_{dp} values are observed slightly before the first lightning, indicating that our case study was likely captured around that time.

The Gamma DSD parameters (Equation 4) can provide further insights into the microphysical characteristics of the rain cells cores. The DSD parameters shown in Figure 10 were obtained from the data of Figure 9 with the following additional filters: 1) elevation angles between 1.8° and 15° in order to minimize both ground noise and effects of high elevation angles on Z_{dr} and K_{dp}; 2) $\mu \leq 6$; and 3) $2 \leq \log(N_w) \leq 6$. DSD parameters outside the range of filters 2 and 3 are primarily associated to higher altitudes and are not central to the discussions here.

As mentioned earlier, the DSD parameters indicate that droplets reach maximum size upon the cell detection, which is accompanied by relatively small concentrations as seen by low N_w. From this point on, the overall trend is for increasing N_w and μ with decreasing D_0. The positioning of the COA seems to have an impact in the overall DSD parameters profiles, not limited only to its layer. A good example can be seen in Figure 10e for Case 1. We note that when COA is high, μ remains relatively constant with altitude. However, when COA starts decaying, μ may increase for $H >$ COA. This is enhanced in the latter stages of Case 2because of the faster COA sedimentation. Therefore, systems that are able to maintain high COA are likely to have relatively big droplets throughout its core (μ is inversely proportional to D_0) and a strong Z_{dr} column, which is also favored when VIL is high (see Table 1 for Case 1).

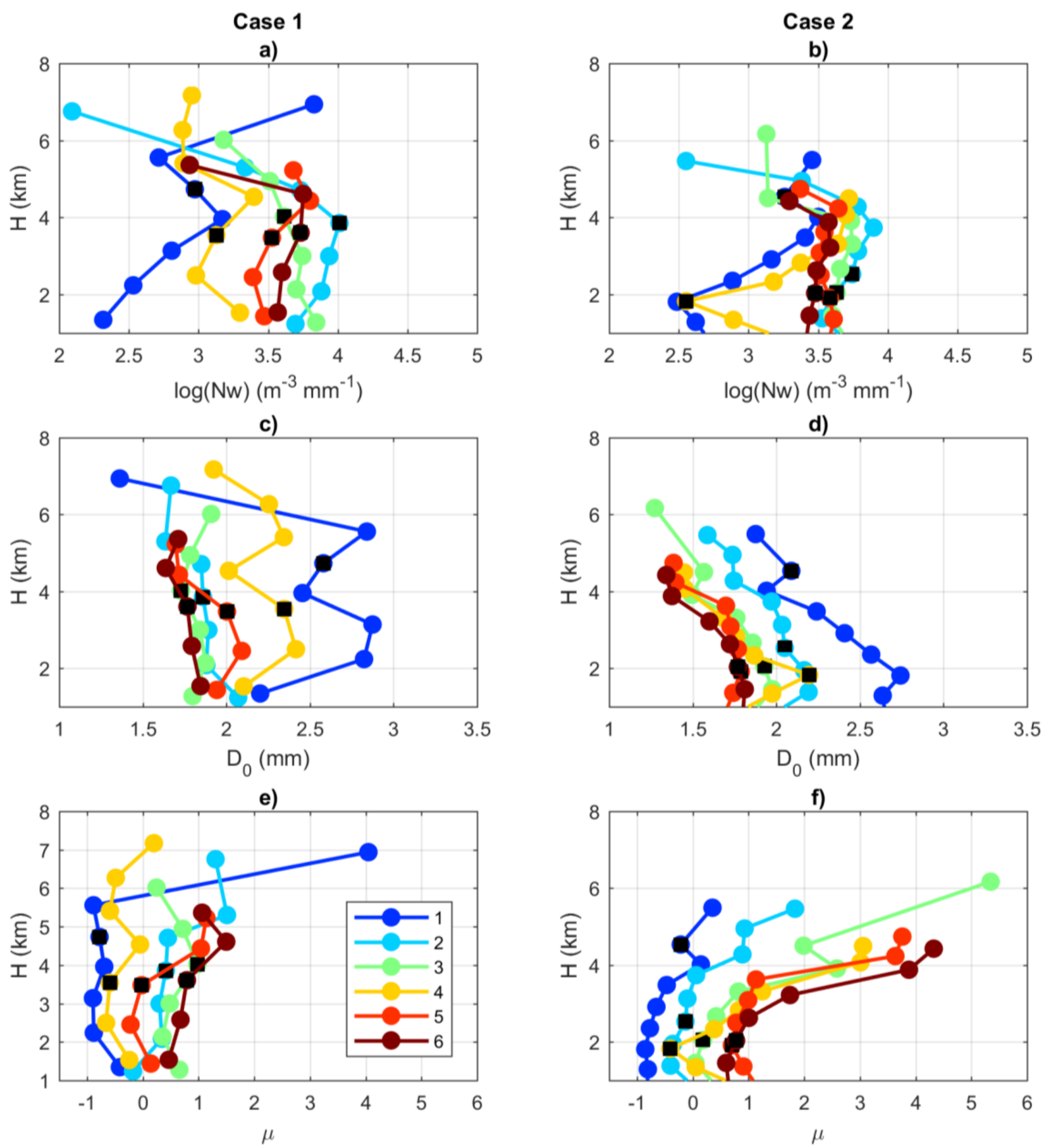

Figure 10: Gamma DSD parameters calculated from the averaged profiles shown in Figure 9 for Case 1 (left column) and Case 2 (right column). Black squares represent the closest datapoint to COA for each time step. Chronological time steps are given in the legend of panel e, where the respective UTC times are given in Table 1.

In terms of the DSDs close to the COA along the rain cells lifecycle (black squares in Figure 10), we note that the case studies presented significantly lower μ and higher D_0 as compared to the medians shown in Figure 8 (taking into account VIL and COA values). The comparison for N_w is not as straightforward because of the change in behavior around VIL = 3 kg m^{-2}, but the case studies usually present more extreme values, be it to the lower or higher end. This observation highlights the difference between the treatment of the systems as a bulk or individually. The overall medians in Figure 8 are necessarily biased towards the most common characteristics, which are often related to relatively weaker cells within the COA and VIL intervals. Therefore, Figure 8 can now be understood as an approximation of the minimum properties a system must have in order to generate enough precipitation at 2 km altitude to be detected by a tracking algorithm such as ForTraCC.

One point in common between Cases 1 and 2 is the presence of negative μ values at COA at detection. As discussed earlier, this point is probably close to the lightning activity initiation and the formation of Z_{dr} columns. Therefore, the evolution of μ at COA throughout the cells lifecycle could also be considered for nowcasting applications.

4 Conclusions

In this study, the macro- and microphysical characteristics of the 2016/7 summer rain cells were explored as part of the SOS-CHUVA experiment. The cells were tracked by the ForTraCC algorithm allowing for the analysis of Lagrangean properties. The cells studied were primarily afternoon convective systems with average duration and area of 29 minutes and 59 km^2, respectively. However, some cells lasted longer and covered larger areas – having 90% percentiles of 1 hour and 127 km^2, respectively. For each cell the calculation of the vertical center of activity (COA) was introduced as a mean to locate the most active layer of the cells in terms of water mass.

It was shown that COA varies mostly between 2 km and 4.5 km and presents positive relations to total cell water (W_T), VIL and DVIL. In order to further understand COA and its relation to the rain cells development, an exploratory analysis was applied to detail its relation to precipitation formation and system development and microphysics.

When the cells are first detected by ForTraCC (using a threshold of 5 mm h^{-1} or 34 dBZ in the 2 km CAPPI), COA is usually around 4 km or 4.5 km. At this point, our results suggest that they are close to their mature stage, right before a sudden increase in the precipitation amounts at 2 km (the lower CAPPI used). Therefore, it shows that mature rain cells usually present high COA, which sediments as they collapse and dissipate. Averaged reflectivity profiles showed that Z is around 44.5 dBZ at the COA level when it is at 4.5 km, diminishing only by 2 dBZ when the cells dissipate with COA at 2.0 km. Therefore, it is possible to follow the bulk of the water within the rain cells by tracking the COA evolution, which is a level of relative balance between collection and evaporation processes.

The COA level was found to be a property shared by rain cells with varying characteristics such as size, average VIL or echo tops. Therefore, it is interesting to add other criteria to study the rain cells. In this study we used VIL together with COA to show overall and specific characteristics of the cells measured during SOS-CHUVA. Contrary to the results mentioned above, we found that the reflectivity at the cells core and at the COA level tend to increase with decreasing COA, given that VIL remains relatively constant. The same was observed for Z_{dr} and K_{dp}, meaning that droplets may continue to grow on the cells cores even during the dissipation stage provided that there is enough background water to support their growth. On the other hand, cells sharing the same COA can present enhanced polarimetric characteristics the higher their VIL is. Therefore, the evolution of observed cells can be understood by the balance between COA and VIL variability. The relatively small variability on the overall averaged Z at COA (i.e. the 2 dBZ mentioned earlier) indicates that the balance between collection and evaporation processes can also be visualized in the VIL-COA approach for the cells measured during SOS-CHUVA.

The microphysical characteristics of the rain cells cores were also analyzed by the respective Gamma DSD parameters. It was shown that the shape parameter μ have an overall median variability between 0.5 and 3.0, associated to a 1.4 mm ≤ D_0 ≤ 1.8 mm interval. The general trend is for increased (decreased) D_0 (μ) for either increasing VIL or decreasing COA. On the other hand, N_w presents a different behavior where it grows with VIL up to VIL = 3 kg m^{-2} where the pattern reverses. This was consistently observed regardless of the COA values.

The case studies shown here provided more details on the relation between overall rain cell vertical structure and the relative COA, as well as providing a comparison between the polarimetric and DSD characteristics within the life cycle to contrast with the overall patterns found. We showed that the high COA observed at the earlier stages of the rain cells life cycles (already close to the mature stage with the thresholds used here) are associated to higher Z, Z_{dr} and K_{dp} in the mixed layer, which indicates: 1) relatively strong updrafts; 2) Z_{dr} column formation; 3) likely the beginning of cells electrification. Those characteristics were also followed by negative μ according to the methodology adopted here. Right after this characteristic profile, there is a sudden increase in the accumulated rain in the 2 km CAPPIs. Therefore, we were able to highlight the rain cells properties that anticipate the onset of the bulk of precipitation in the lower levels. This may be used in the future as a frame of reference for new studies and to operational applications. We highlight that the COA measure does not rely on polarimetric retrievals meaning that it can provide additional insights into the rain cells properties even for single-polarization radars.

Acknowledgments

We would like to thank the entire SOS-CHUVA team for their work in preparing and executing the project that allowed this study. SOS-CHUVA was funded under project grant FAPESP 2015/14497-0. Micael A. Cecchini was supported by FAPESP grant number 2017/04654-6.

The data used in this study can be found at: http://chuvaproject.cptec.inpe.br/portal/noticia.ultimas.logic?i=en

The authors declare that there is no conflict of interests regarding this publication.

References

Beyer, J. L. (1974). Global summary of human response to natural hazards: floods. In: G. F. White (Ed.), *Natural Hazards: Local, National, Global* (pp. 265-273). New York, NY: Oxford University Press.

Calheiros, A. J. P., & Machado, L. A. T. (2014). Cloud and rain liquid water statistics in the CHUVA campaign. *Atmos. Res.*, 144**,** 126–140. doi:10.1016/j.atmosres.2014.03.006,.

Carlin, J.T., Gao, J., Snyder, J.C., & Ryzhkov, A.V. (2017). Assimilation of Z_{DR} Columns for Improving the Spinup and Forecast of Convective Storms in Storm-Scale Models: Proof-of-Concept Experiments. *Mon. Wea. Rev.*, 145, 5033–5057. doi:10.1175/MWR-D-17-0103.1.

Cecchini, M. A., Machado, L. A. T., Wendisch, M., Costa, A., Krämer, M., Andreae, M. O., et al. (2017). Illustration of microphysical processes in Amazonian deep convective clouds in the gamma phase space: introduction and potential applications. *Atmos. Chem. Phys.*, 17, 14727-14746. https://doi.org/10.5194/acp-17-14727-2017.

Chen, Q., Koren, I., Altaratz, O., Heiblum, R. H., Dagan, G., & Pinto, L. (2017). How do changes in warm-phase microphysics affect deep convective clouds?. *Atmos. Chem. Phys.*, 17, 9585-9598. https://doi.org/10.5194/acp-17-9585-2017.

Dagan, G., Koren, I., & Altaratz, O. (2018). Quantifying the effect of aerosol on vertical velocity and effective terminal velocity in warm convective clouds. *Atmos. Chem. Phys.*, 18, 6761-6769. https://doi.org/10.5194/acp-18-6761-2018.

Heiblum, R. H., Altaratz, O., Koren, I., Feingold, G., Kostinski, A. B., Khain, A. P., et al. (2016a). Characterization of cumulus cloud fields using trajectories in the center-of-gravity vs. water mass phase space: 1. Cloud tracking and phase space description. *J. Geophys. Res.*, 121, 6336–6355. https://doi.org/10.1002/2015JD024186.

Heiblum, R. H., Altaratz, O., Koren, I., Feingold, G., Kostinski, A. B., Khain, A. P., et al. (2016b). Characterization of cumulus cloud fields using trajectories in the center of gravity versus water mass phase space: 2. Aerosol effects on warm convective clouds. *J. Geophys. Res.*, 121, 6356–6373. https://doi.org/10.1002/2015JD024193.

Hubbert, J., & Bringi, V.N. (1995). An Iterative Filtering Technique for the Analysis of Copolar Differential Phase and Dual-Frequency Radar Measurements. *J. Atmos. Oceanic Technol.*, 12, 643–648. https://doi.org/10.1175/1520-0426(1995)012<0643:AIFTFT>2.0.CO;2.

Kalogiros, J., Anagnostou, M. N., Anagnostou, E. N., Montopoli, M., Picciotti, E. & Marzano, F. S. (2013). Optimum estimation of rain microphysical parameters from X-band dual-polarization radar observables. *IEEE Trans. Geosci. Remote Sens.*, 51(5), 3063–3076. doi:10.1109/TGRS.2012.2211606.

van Lier-Walqui, M., Fridlind, A.M., Ackerman, A.S., Collis, S., Helmus, J., MacGorman, D.R., et al. (2016). On Polarimetric Radar Signatures of Deep Convection for Model Evaluation: Columns of Specific Differential Phase Observed during MC3E. *Mon. Wea. Rev.*, 144, 737–758. https://doi.org/10.1175/MWR-D-15-0100.1.

Machado, L.A. & Laurent, H. (2004). The Convective System Area Expansion over Amazonia and Its Relationships with Convective System Life Duration and High-Level Wind Divergence. *Mon. Wea. Rev.*, 132, 714–725, https://doi.org/10.1175/1520-0493(2004)132<0714:TCSAEO>2.0.CO;2.

Machado, L. A. T., Silva Dias, M. A. F., Morales, C., Fisch, G., Vila, D., Albrecht, R. I., et al. (2014). The Chuva Project: How Does Convection Vary across Brazil?. *B. Am. Meteorol. Soc.*, 95, 1365–1380. https://doi.org/10.1175/BAMS-D-13-00084.1.

Martins, J. A., Brand, V. S., Capucim, M. N., Felix, R. R., Martins, L. D., Freitas, E. D., et al. (2017). Climatology of destructive hailstorms in Brazil. *Atmos. Res.*, 184, 126–138. doi:10.1016/j.atmosres.2016.10.012.

Mattos, E. V., Machado, L. A. T., Williams, E. R., & Albrecht, R. I. (2016). Polarimetric radar characteristics of storms with and without lightning activity. *J. Geophys. Res. Atmos.*, 121, 14,201–14,220. doi:10.1002/2016JD025142.

Mattos, E. V., Machado, L. A. T., Williams, E. R., Goodman, S. J., Blakeslee, R. J., & Bailey, J. C. (2017). Electrification life cycle of incipient thunderstorms. *J. Geophys. Res. Atmos.*, 122, 4670–4697. doi:10.1002/2016JD025772.

Queiroz, A. P. (2009). *Monitoramento e previsão imediata de tempestades severas usando dados de radar* (master's thesis). Retrieved from INPE-14181- TDI/1093 (http://urlib.net/sid.inpe.br/mtc-m18@80/2008/11.17.19.50). São José dos Campos, SP: Instituto Nacional de Pesquisas Espaciais.

Stevaux, J., Latrubesse, E., Hermann, M., & Aquino, S. (2009). Floods in urban areas of Brazil. *Dev Earth Surf Process*, 13:245–266. doi:10.1016/S0928-2025(08)10013-X.

Testud, J., Le Bouar, E., Obligis, E., & Ali-Mehenni, M. (2000). The Rain Profiling Algorithm Applied to Polarimetric Weather Radar. *J. Atmos. Oceanic Technol.*, 17, 332–356. https://doi.org/10.1175/1520-0426(2000)017<0332:TRPAAT>2.0.CO;2.

Vila, D. A., Machado, L. A. T., Laurent, H. & Velasco, I. (2008). Forecast and Tracking the Evolution of Cloud Clusters (ForTraCC) Using Satellite Infrared Imagery: Methodology and Validation. *Weather Forecast*, 23(2), 233–245. doi:10.1175/2007WAF2006121.1.

Yuter, S. E., & Houze Jr., R. A. (1995). Three-dimensional kinematic and microphysical evolution of Florida cumulonimbus. Part II: Frequency distributions of vertical velocity, reflectivity, and differential reflectivity. *Mon. Wea. Rev.*, 123, 1941–1963. doi:10.1175/1520-0493(1995)123,1941:TDKAME.2.0.CO;2.